

Orbitally driven changes in seasonal Antarctic temperature during the Holocene

Tyler Jones (✉ Tyler.Jones@Colorado.edu)

Institute of Arctic and Alpine Research, University of Colorado <https://orcid.org/0000-0003-1871-2105>

Bradley Markle

University of Colorado Boulder

William Roberts

Northumbria University

Kurt Cuffey

UC Berkeley

Eric Steig

University of Washington <https://orcid.org/0000-0002-8191-5549>

Christopher Stevens

University of Washington

Paul Valdes

Bristol University <https://orcid.org/0000-0002-1902-3283>

T.J. Fudge

University of Washington <https://orcid.org/0000-0002-6818-7479>

Michael Sigl

University of Bern Oeschger Centre for Climate Change Research <https://orcid.org/0000-0002-9028-9703>

Abigail Hughes

University of Colorado

Joshua Garland

Santa Fe Institute <https://orcid.org/0000-0002-6724-2755>

Bo Vinther

Center for Ice and Climate, University of Copenhagen

Kevin Rozmiarek

University of Colorado

Chloe Brashear

University of Colorado

James White

Institute of Arctic and Alpine Research, University of Colorado

Physical Sciences - Article

Keywords: mean annual temperature change, seasonal temperature change, Antarctica, Holocene

Posted Date: June 11th, 2021

DOI: <https://doi.org/10.21203/rs.3.rs-564788/v1>

License:  This work is licensed under a Creative Commons Attribution 4.0 International License.

[Read Full License](#)

1 **Orbitally driven changes in seasonal Antarctic temperature during the Holocene**

2
3 Tyler R. Jones^{1*}, Bradley R. Markle^{1,2}, William H. G. Roberts³, Kurt M. Cuffey⁴, Eric J. Steig⁵, C. Max Stevens^{6,7}, Paul J.
4 Valdes⁸, T. J. Fudge⁵, Michael Sigl⁹, Abigail G. Hughes², Joshua Garland¹⁰, Bo M. Vinther¹¹, Kevin S. Rozmiarek², Chloe A.
5 Brashear², James W. C. White²
6

7 ¹ Institute of Arctic and Alpine Research, University of Colorado, Boulder, CO 80309, USA

8 ² Department of Geological Sciences, University of Colorado, Boulder, CO 80309, USA

9 ³ Geography and Environmental Sciences, Northumbria University, Newcastle, UK

10 ⁴ Department of Geography, University of California, Berkeley, CA 94720, USA

11 ⁵ Department of Earth and Space Sciences, University of Washington, Seattle, WA 98195, USA

12 ⁶ Cryospheric Science Laboratory, NASA Goddard Space Flight Center, Greenbelt, MD, USA

13 ⁷ Earth System Science Interdisciplinary Center, University of Maryland, College Park, MD, USA

14 ⁸ School of Geographical Sciences, University of Bristol, Bristol, UK

15 ⁹ Climate and Environmental Physics, Physics Institute & Oeschger Centre for Climate Change Research, University of Bern,
16 Bern, Switzerland

17 ¹⁰ Santa Fe Institute, Santa Fe, NM 87501, USA

18 ¹¹ Centre for Ice and Climate, Niels Bohr Institute, University of Copenhagen, Denmark

19
20 *corresponding author: Tyler Jones (tyler.jones@colorado.edu)
21

22 **Disentangling the drivers of mean annual temperature change in Antarctica requires an understanding of**
23 **seasonal temperature change. A high-resolution climate record capable of resolving summer and winter**
24 **seasons could address long-standing questions about the role of orbitally-driven insolation in driving**
25 **Antarctic mean-annual temperature change. Here, we present a continuous record of water isotope ratios**
26 **from the West Antarctic Ice Sheet (WAIS) Divide ice core that reveals both summer and winter temperature**
27 **change though the last 11,000 years. This novel record shows that summer temperatures increased through**
28 **the early-to-mid Holocene, reached a plateau at 4 to 2 ka, and then decreased to the present. The observed**
29 **changes are explained primarily by changes in maximum summer insolation. In the early to mid-Holocene,**
30 **additional summer warming results from the retreat and thinning of the WAIS. The magnitude of summer**
31 **temperature change constrains the lowering of the WAIS surface to less than 100 m since the early Holocene,**
32 **consistent with geologic records. Importantly, annual mean temperatures cannot be fully explained by orbital**
33 **forcing and ice sheet elevation change alone; in the early Holocene, large wintertime temperature excursions**
34 **overwhelm the summer signal. These winter excursions indicate that regional heat transport anomalies,**
35 **rather than local thermodynamics, can dominate the annual mean.**
36

37 Orbitally-driven changes in insolation are the most important external forcing of the climate system. In addition to
38 pacing the ice ages by influencing the mass balance of Northern Hemisphere ice sheets (e.g. Roe 2006), these
39 changes directly influence the climate at all latitudes by altering the seasonal energy balance. Many studies have
40 sought to understand the influence of orbital change on Antarctic climate. For example, summer duration – the
41 number of days above an insolation threshold of 250 Wm^{-2} – covaries with mean annual temperature on glacial-
42 interglacial timescales (Huybers and Denton 2008). Similarly, integrated summer insolation is thought to have
43 contributed to the mean temperature increase at the initiation of the deglaciation in West Antarctica (WAIS Divide
44 Project Members 2013). These studies are driven by the interpretation of proxy records that have only annual mean
45 or lower resolution. Yet, the fundamental mechanism behind orbital forcing is changes to the seasonal cycle of

46 insolation, which drives changes in the seasonality of climate. Large variance in one season, but not the other, would
47 disproportionately affect the annual mean. In this study, we resolve seasonal temperatures in West Antarctica to
48 understand how orbital forcing (which is fundamentally seasonal) directly influences seasonal and mean Antarctic
49 temperature.

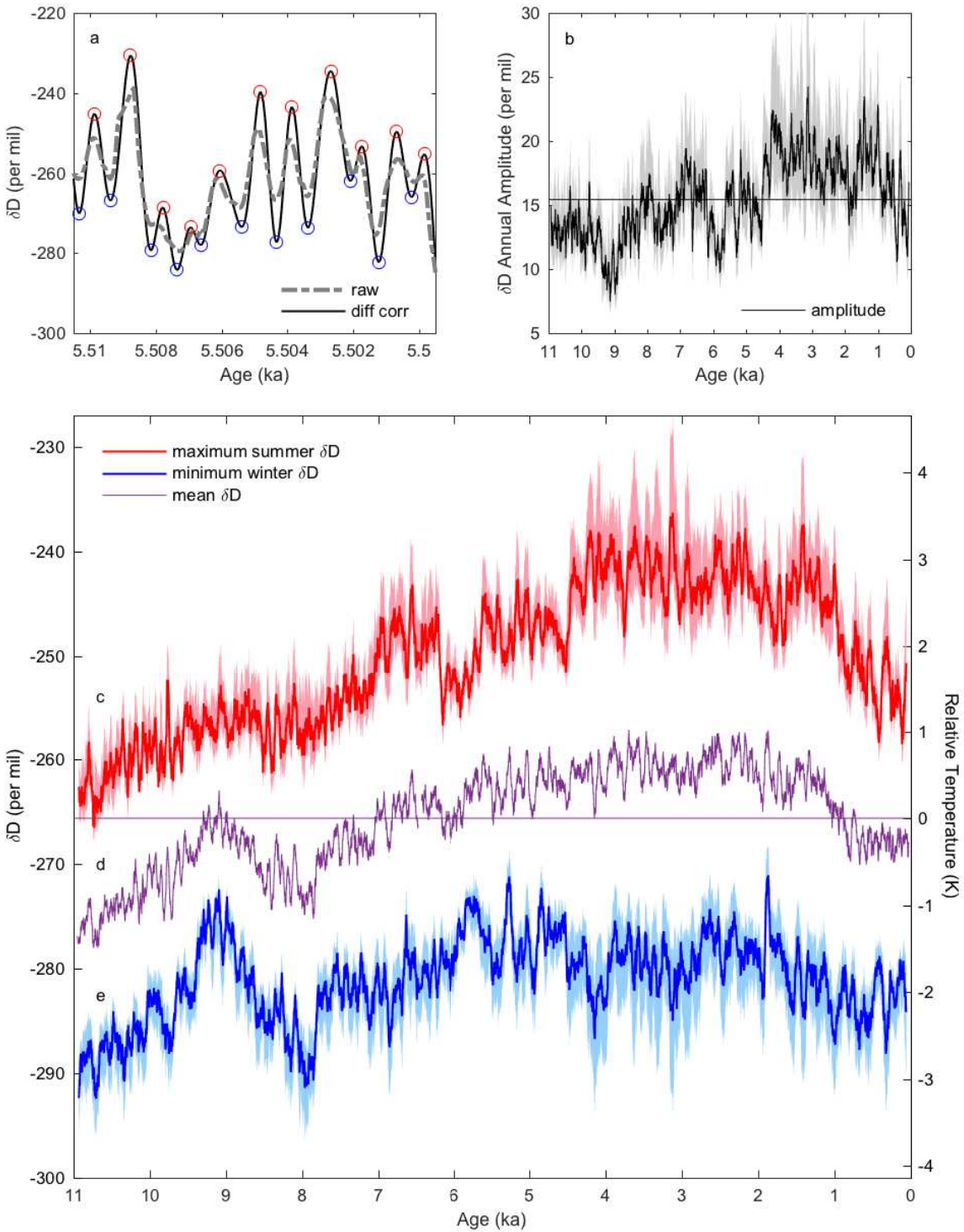
50

51 We reconstruct seasonal and annual temperature variability in West Antarctica through the Holocene (last 11,000
52 years) using the high-resolution water isotope record from the West Antarctic Ice Sheet (WAIS) Divide ice core
53 (WDC) (Jones et al. 2018, White et al. 2019, Jones et al. 2020) (ED Figure 1a,b). The WDC record was obtained
54 with a continuous-flow technique (Jones et al. 2017a) that provides unprecedented millimeter-scale depth resolution
55 and sub-seasonal temporal resolution (see Methods). Annual dating is available to 31 ka (WAIS Divide Project
56 Members 2013; Sigl et al. 2016); the full record extends to 68 ka (WAIS Divide Project Members 2015). The
57 accumulation rate at WAIS Divide is sufficiently high that sub-annual information is resolved in the ice core through
58 the entire Holocene (Jones et al. 2017b). Correction for diffusion using spectral techniques (Johnsen et al. 2000,
59 Vinther et al. 2003; see Methods), allows us to recover and quantify variations in both summer maxima and winter
60 minima for each year (Figure 1a). More snowfall in one season than another enhances diffusional smoothing of the
61 drier season, introducing preservation bias. We quantify the magnitude of this effect, and find that the effect is small
62 (see Methods). We take advantage of the covariance of water isotopes with local temperature at seasonal and longer
63 timescales (Jouzel et al. 1997, Küttel et al. 2012, Steig et al. 2013). We use a temperature sensitivity for δD of 8.3
64 $\text{‰}/^\circ\text{C}$ (Cuffey et al., 2016; Markle and Steig, in review 2021).

65

66 Summer temperature at WAIS Divide (Figure 1c) varied by 2.5°C across the Holocene, while winter temperature
67 (Figure 1e) varied by 2°C in the early Holocene and by $<0.5^\circ\text{C}$ in the mid-to-late Holocene. Summer temperature
68 generally increases from ~ 11 to 4.2 ka, reaching maximum values between ~ 4.2 and 1.4 ka, and then decreases
69 toward the present. The evolution of summer temperature exhibits the same pattern as local maximum insolation,
70 rather than the duration of summer (Figure 2e). Compared to summer, the winter variability is more subdued,
71 except for two prominent features: a pronounced peak at ~ 9.2 ka and subsequent cooling to ~ 7.9 ka, the minimum of
72 the entire record. The 9.2-ka peak represents one of the warmest winter intervals in the Holocene, corresponding to
73 an increase of 1.0°C above the mean. The early-Holocene winter variability occurs at frequencies too high to be
74 attributable to orbital forcing, and may instead reflect changes in meridional heat transport. Annual amplitudes (half
75 the summer-winter difference) are up to 2.5 times larger in the late Holocene compared to the early Holocene
76 (Figure 1b). The mean temperature (Figure 1d) is dominated by winter variability in the early Holocene, and by the
77 larger range of summer variability in the mid-to-late Holocene.

78

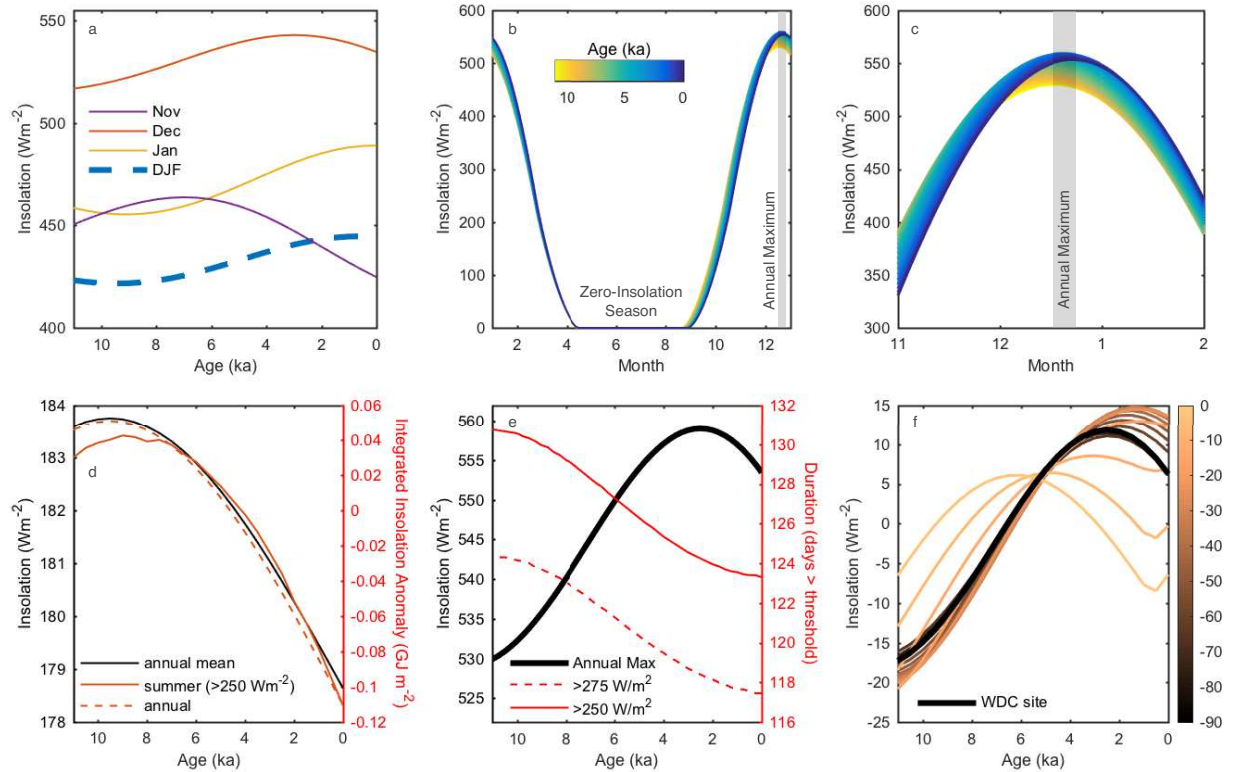


79

80 **Figure 1 | Water isotope seasonal variability.** *a*, The diffusion-corrected (solid line) and raw (dashed line) WDC
 81 δD records, with annual maxima (red circles) and minima (blue circles) determined by an algorithm (see Methods).
 82 The full high-resolution WDC δD record, quantified diffusion lengths, and maximum and minimum picks are shown
 83 in Extended Data Figure 1. *b*, Annual amplitude; the horizontal line is the Holocene mean. *c*, *d*, *e*, 50-yr δD
 84 averages for summer (red), the mean (purple), and winter (blue); the horizontal line is the Holocene mean; the
 85 shaded regions are 1σ uncertainty bounds. We use an isotope-temperature scaling ($d\delta D/dT_{surf}$) of $8.3\text{‰}/^{\circ}\text{C}$ (Markle
 86 and Steig in review, 2021).

87 To estimate the extent to which the temperature reconstructions in Figure 1 can be explained by orbitally-driven
88 insolation change, we use a global, zonal-mean (2° resolution) moist energy balance model (MEBM; see Methods)
89 which accounts for incoming and outgoing radiation, albedo, and meridional atmospheric heat transport. With the
90 MEBM, we first investigated seasonal changes in the radiative equilibrium temperature, forced directly by insolation
91 changes accompanying the slow changes of Earth's orbital parameters (Figure 3a; ED Figure 5), calculated
92 (Huybers, 2011) for TOA at 80°S . Maximum summer insolation increases over the Holocene and peaks at ~ 2.5 ka
93 (Figure 2b,c,e), while the annual mean and the annual and summer integrated values mostly decline over the same
94 interval (Figure 2d). Due to the absence of winter insolation south of the Antarctic Circle, the amplitude of seasonal
95 insolation follows the long-term changes in maximum summer insolation. The MEBM results (Figure 3) are
96 straightforward: at the latitude of the WDC site, summer maximum temperatures, mean summer (DJF) temperatures,
97 and the magnitude of the seasonal temperature cycle, all covary with maximum summer insolation (Figure 2e,f).
98 Local maximum summer insolation is the dominant driver of changes in local summer temperature in the MEBM.
99 While heating at lower latitudes also influences Antarctic temperature through atmospheric heat transport, maximum
100 summer temperatures at WDC correlate best to local insolation rather than insolation at any lower latitude (Figure
101 2f). Moreover, changes in summer heat convergence during the Holocene act in the opposite direction and are too
102 small in magnitude compared to local insolation (ED Figure 6e,f). Because December is always the month of
103 maximum insolation, much greater than neighboring months (Figure 2), variability of December insolation
104 dominates the response of maximum summer temperature. Modeled winter temperatures are less variable than
105 summer temperatures at 80°S (Figure 3a) due to the lack of direct insolation. The winter minima are a function of
106 three factors: changes in the length of the zero-insolation season, the effective cooling rate of the surface, and heat
107 transport from lower latitudes. At times when the zero-insolation season is longer, winter minimum temperatures are
108 lower, as expected. However neither the length of the zero insolation season nor modeled winter minimum
109 temperatures correlate well with the observed variations in winter temperature minima.

110



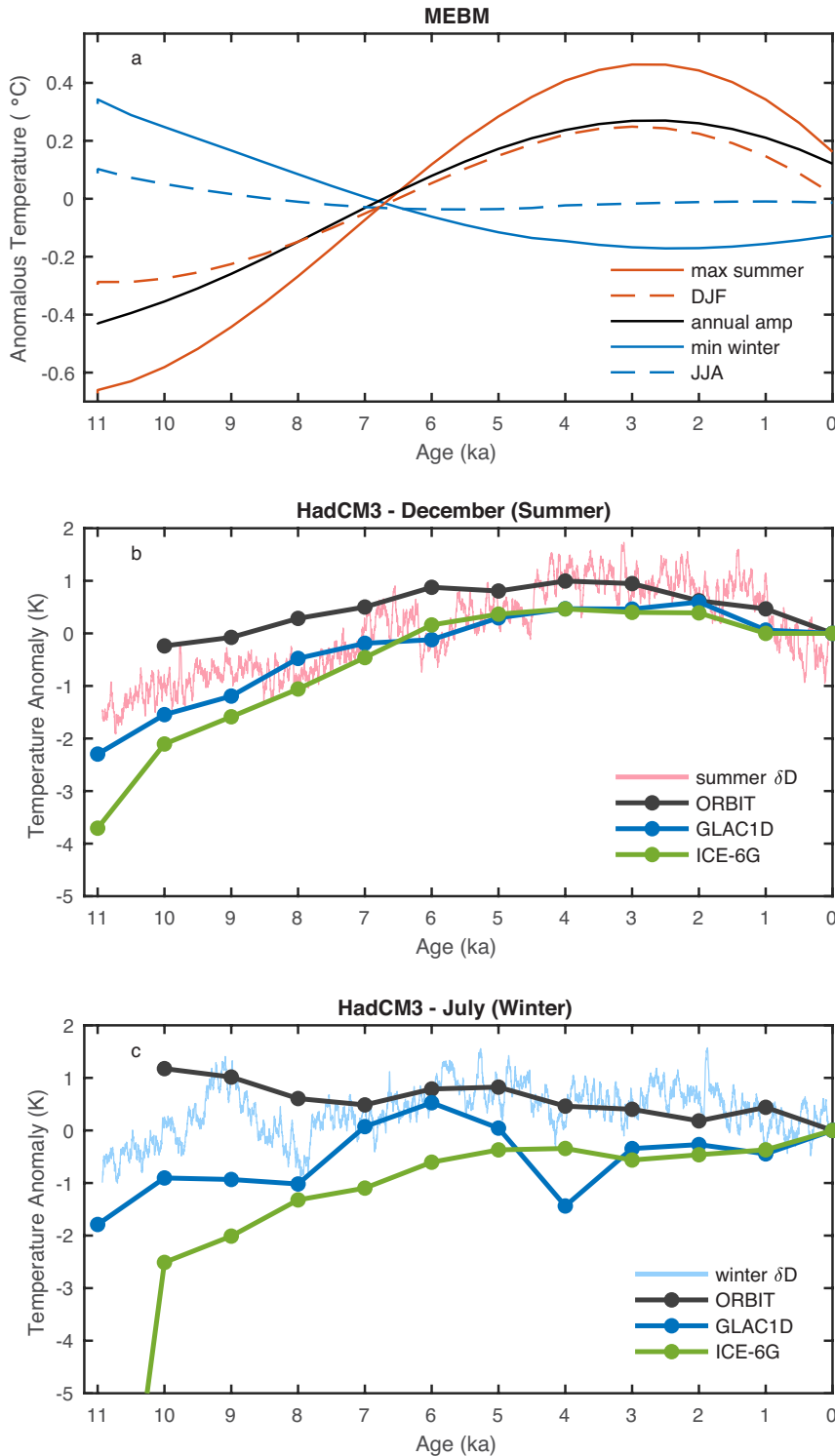
112

113 **Figure 2 | Temporal and Spatial Variability in Insolation.** *a*, Insolation change through the Holocene for
 114 different months and the austral summer season (DJF). *b*, The full seasonal cycle of insolation at 80°S for 500-yr
 115 snapshots over the Holocene. Line colors in (*a*) and (*b*) correspond to age. *c*, Zoom in of summer insolation. The
 116 maximum insolation value always occurs in December (grey shading), migrating across 8 days over the course of
 117 the Holocene. *d*, Change through the Holocene for the annual mean (black), annual integrated (dashed red line),
 118 and summer integrated (red line) insolation. *e*, Maximum summer insolation (i.e. maximum intensity; black line) and
 119 summer duration (dashed red lines) defined as the number of days above a threshold insolation value each year. *f*,
 120 Anomaly in maximum insolation colored by latitude in the Southern Hemisphere. The thick black line shows the
 121 latitude of the WDC site.

122

123 To investigate the possible role of more-complex mechanisms, including topographical changes not accounted for in
 124 the MEBM, we simulated Holocene climate with a fully-coupled general circulation model, HadCM3 (Singarayer
 125 and Valdes 2010, see Methods). Simulations forced solely by changes in orbital parameters (ORBIT; Figure 3b)
 126 produces December maximum temperatures at 80°S with the same pattern as for the simpler model: increasing over
 127 the Holocene, peaking between 4 to 2 ka, and decreasing into the modern. As with the MEBM, this result arises
 128 directly from the pattern of maximum summer insolation and matches well with the observed summer temperature
 129 signal. Agreement between WDC observations and both models indicates that the large orbitally-driven changes in
 130 maximum summer insolation dictate the summer temperature response in West Antarctica (Figure 3b). In contrast,
 131 the wintertime response of both models to orbital forcing (Figure 3c) – cooling from early Holocene to the present –
 132 is inconsistent with observed winter temperatures.

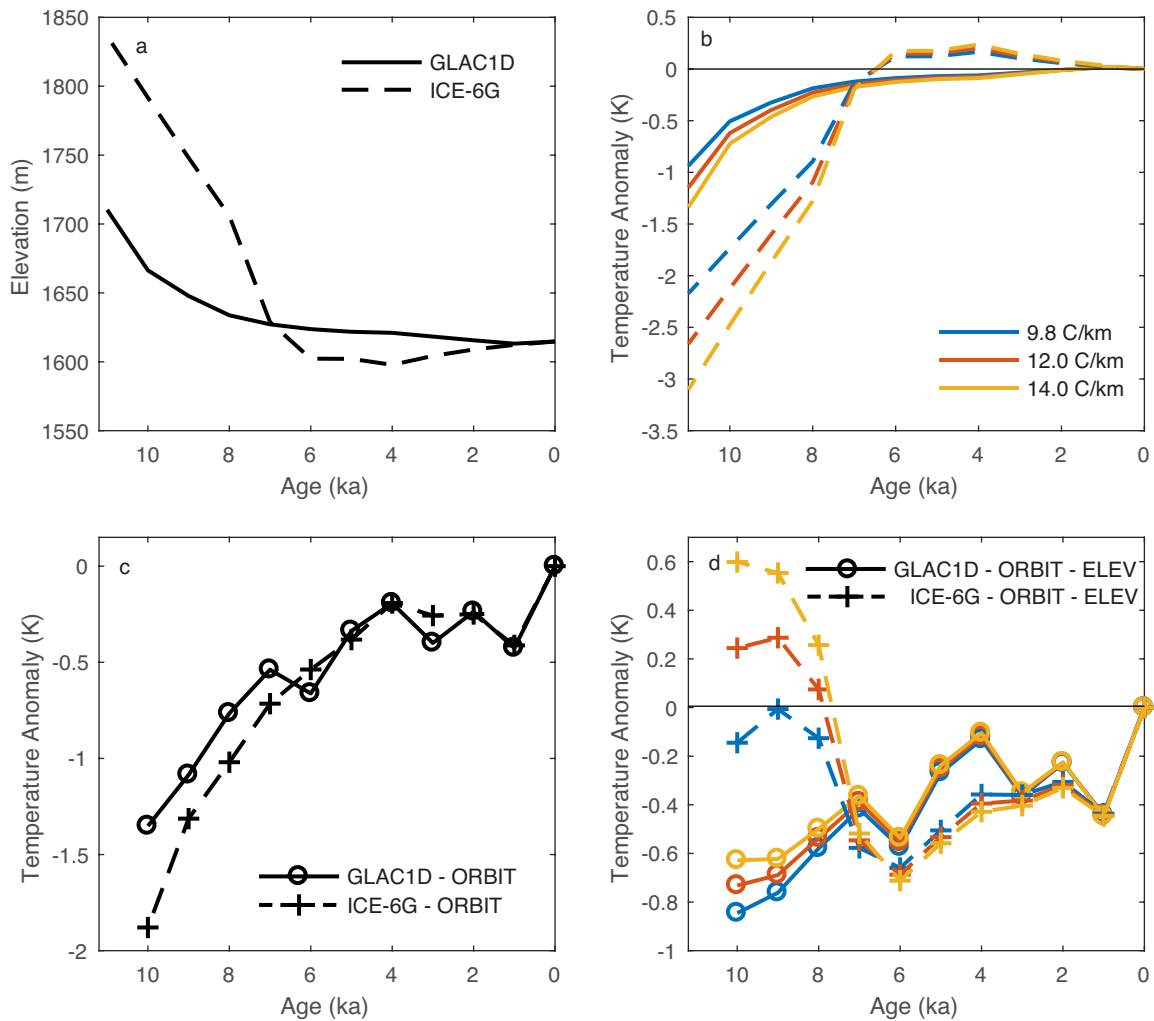
133



134
 135 **Figure 3 | Model Results.** *a*, Temperature estimations for 80°S using the Moist Energy Balance Model (MEBM),
 136 including maximum summer intensity (red), DJF (red dashed), base winter intensity (blue), JJA (blue dashed), and
 137 the amplitude of the seasonal temperature cycle (black). *b-c*, HadCM3 zonal results for 80°S compared to observed
 138 summer and winter δD (Figure 1), normalized to 0 ka. *b*, December (summer), *c*, July (winter).
 139

140 While the temporal pattern of summer temperature clearly covaries with insolation, the magnitude of that
141 temperature response is not fully explained by insolation change. The results of the MEBM and HadCM3 orbitally-
142 forced simulation underestimate by a factor of two the total amplitude of maximum summer temperature change
143 over the whole Holocene, perhaps indicating the importance of ice-sheet elevation changes or evolving greenhouse-
144 gas forcing. To address this, we investigated the effect of two different ice sheet histories (GLAC1D and ICE-6G,
145 Figure 4a), prescribed as boundary conditions to the HadCM3 simulations. From 11 to 3 ka, GLAC1D and ICE-6G
146 impose a reduction of ice sheet elevation by 96 m and 222 m, respectively, at the WDC site. With changes to the ice
147 sheet included, HadCM3 simulates a larger range in maximum summertime temperatures. The temperature effect
148 from ice sheet elevation exhibits the same general temporal pattern as summer insolation: maximum cooling in early
149 Holocene followed by a warming trend. Much of the elevation-induced warming can be attributed directly to the
150 surface lapse-rate effect (Figure 4b), but comparison to the orbital-only runs (Figure 4c,d) reveals a remaining
151 temperature anomaly, attributable to greenhouse gases and to interactions between the model's responses to
152 simultaneously-imposed forcings. The interactions are highly non-linear; for example, the residuals during the early-
153 Holocene (11-6 ka) are of the opposite sign for GLAC1D and ICE-6G (Figure 4d).

154



155
 156 **4 | Possible ice elevation histories and the corresponding temperature histories from climate model**
 157 **simulations. a,** The elevation histories used in HadCM3. **b,** The temperature anomalies from elevation change
 158 (GLAC1D solid lines; ICE-6G dashed lines) using an atmospheric lapse rate of 9.8°C/km, and spatial lapse rates
 159 for interior West Antarctica of 12°C/km (Masson-Delmotte et al. 2008) and 14°C/km (Fortuin and Oerlemans,
 160 1990). **c,** HadCM3 residual-temperature anomalies for December (summer) calculated by subtracting the ORBIT
 161 run from the GLAC1D and ICE-6G runs (the runs are shown in Figure 3c), highlighting what is attributable to the
 162 ice sheet elevation forcing rather than from changes in insolation. **d,** The residual temperature change in (b)
 163 subtracted from the results in (c), showing what may be driven from processes besides the direct lapse rate effect
 164 and orbital forcing.

165
 166 Comparison of insolation-driven summer warming diagnosed by the MEBM and HadCM3 with the magnitude of
 167 summer warming implied by our ice-core record constrains Holocene elevation changes of the West Antarctic Ice
 168 Sheet. Both models predict an orbitally-forced rise of ~1.25°C from 11-3ka compared to 2.5°C from δD (using
 169 1,000-yr averaging to remove centennial-scale noise). The residual 1.25°C in δD would require 125 m lowering of
 170 the ice sheet surface, if the effect arises purely from the free-atmosphere adiabatic lapse rate, of magnitude
 171 0.98°C/100m. With attendant changes of greenhouse gases, zonal heat transport, and downward longwave radiation,
 172 an even smaller lowering is needed (ED Figure 7). A close match to observed summer temperature anomalies is

173 obtained using the HadCM3 model and GLAC1D elevation scenario (Figure 3b). This indicates that the WAIS
174 likely lowered by less than 100 m throughout the Holocene, consistent with geological constraints (Ackert et al.
175 1999; Steig et al. 2001, Ackert et al. 2007) and some reconstructed elevation histories (Steig et al. 2001, Cuffey et
176 al. 2016). Our conclusion is also consistent with numerical ice-dynamics models of WAIS that simulate last
177 deglacial retreat in large ensemble runs (those with a basal sliding coefficient in modern oceanic areas of $>10^{-5}$ m
178 $\text{a}^{-1} \text{Pa}^{-2}$) (Pollard et al. 2015).

179
180 MEEM and HadCM3 modeled winter temperatures decrease through the Holocene, owing to the increasing length
181 of the zero-insolation season, but this trend is opposite to the trend in the ice core data. Lapse rate effects associated
182 with a lower ice sheet (Figure 4b) should impact both winter and summer seasons, which can account for the
183 observed upward trend in winter temperature from 11 to 6 ka. This cannot, however, explain the prominent
184 millennial-scale changes at ~ 9.2 and ~ 7.9 ka (Figure 1e). Winter temperatures in West Antarctica are strongly
185 affected by horizontal heat transport by the time-mean atmospheric circulation. Raising the topography of Antarctica
186 tends to reduce such heat transport (ED Figure 7), producing an additional cooling on top of a pure lapse rate effect
187 (Steig et al. 2015). Changing the size and shape of Antarctica is not the only way to alter this heat transport,
188 however. The characteristic “split-jet” structure of the wintertime South Pacific circulation, which influences heat
189 transport to West Antarctica (Chiang et al. 2014), is affected by sea surface temperatures (SST) (Inatsu and Hoskins,
190 2004), mid-latitude SST (Ogawa et al. 2016), North Atlantic SST (Chiang et al. 2014), the Asian monsoon
191 (Nakamura and Shrimpo 2004), and the shape of Antarctica (Patterson et al. 2020, Goyal et al. 2020). The peak in
192 wintertime temperatures at 9.2 ka or the minimum at 7.9 ka may relate to climatic shifts in any of these regions. For
193 example, the surprising wintertime warming at 9.2 ka in West Antarctica may have been associated with regional
194 climate changes that helped initiate abrupt thinning of southern Transantarctic Mountain glaciers from 9-8 ka, which
195 delivered ice to the central Ross Sea and coincided with deglaciation of the Scott Coast (Spector et al. 2017).
196 Perhaps relevant is that the largest Holocene collapse of the East Asian monsoon also occurred at ~ 9.2 ka (Zhang et
197 al. 2018), and that small changes of SST in the tropical Pacific can produce a large response in West Antarctica
198 (Ding et al. 2011). The intricacies of interpreting the early Holocene winter variability in West Antarctica and
199 related teleconnections necessitates further study. In the mid-to-late Holocene, there is very little change in winter
200 temperature in West Antarctica, suggesting more subdued variability of Southern Hemisphere atmospheric
201 circulation than during the early Holocene.

202
203 Milankovitch postulated that long-term variations of Earth’s orbit and axis drive changes in climate over tens of
204 thousands of years by altering the seasonal cycle of insolation. While clearly the main determinant of Northern
205 Hemisphere ice sheet mass balance and global ice volume on glacial-interglacial timescales (e.g. Roe 2006), these
206 astronomical changes also influence atmospheric heating and temperature locally and combine with regional
207 dynamics to create complex influences on the climate system (Huybers 2011). The Holocene provides a window of
208 time to examine the influence of orbital forcing without the complications associated with Northern Hemisphere
209 deglaciation (Jones et al. 2018). Our analysis reveals that West Antarctic summer temperature was primarily

210 controlled by maximum summer local insolation. The large variance of summer temperatures dominates mean
211 temperatures since the mid Holocene. In contrast, winter temperature variations dominate mean temperature changes
212 during the early Holocene; we suggest meridional heat transport is the most important factor. Changes in the
213 topography of the ice sheet, and the resulting surface lapse rate, influence both seasons. Thanks to the high-
214 resolution record used in this study, the differing seasonal dynamics and topographical effects are evident, and the
215 seasonal determinants of mean temperature can be quantified. Seasonal climate dynamics similar to these during the
216 Holocene in West Antarctica, superimposed on glacial-interglacial cycles, must occur in earlier periods.

217 **References**

- 218 Roe, G. (2006). In defense of Milankovitch. *Geophysical Research Letters*, 33(24).
- 219
- 220 Huybers, P., & Denton, G. (2008). Antarctic temperature at orbital timescales controlled by local summer
221 duration. *Nature Geoscience*, 1(11), 787-792.
- 222
- 223 WAIS Divide Project Members (2013). Onset of deglacial warming in West Antarctica driven by local orbital
224 forcing. *Nature*, 500(7463), 440-444.
- 225
- 226 Jones, T. R., Roberts, W. H. G., Steig, E. J., Cuffey, K. M., Markle, B. R., & White, J. W. C. (2018). Southern
227 Hemisphere climate variability forced by Northern Hemisphere ice-sheet topography. *Nature*, 554(7692), 351-355.
- 228
- 229 White, J. W. C. et al. (2019) "Stable Isotopes of Ice in the Transition and Glacial Sections of the WAIS Divide Deep
230 Ice Core" U.S. Antarctic Program (USAP) Data Center. doi: <https://doi.org/10.15784/601274>.
- 231
- 232 Jones, T. R. et al. (2020) "Mid-Holocene high-resolution water isotope time series for the WAIS Divide ice core".
233 U.S. Antarctic Program (USAP) Data Center. doi: <https://doi.org/10.15784/601326>.
- 234
- 235 Jones, T. R., White, J. W. C., Steig, E. J., Vaughn, B. H., Morris, V., Gkinis, V., Markle, B. R., & Schoenemann, S.
236 W. (2017a) Improved methodologies for continuous-flow analysis of stable water isotopes in ice cores, *Atmos.*
237 *Meas. Tech.*, 10, 617–632, <https://doi.org/10.5194/amt-10-617-2017>.
- 238
- 239 Sigl, M., Fudge, T. J., Winstrup, M., Cole-Dai, J., Ferris, D., McConnell, J. R., Taylor, K.C., Welten, K. C.,
240 Woodruff, T. E., Adolphi, F., Bisiaux, M., Brook, E. J., Buizert, C., Caffee, M. W., Dunbar, N. W., Edwards, R.,
241 Geng, L., Iverson, N., Koffman, B., Layman, L., Maselli, O. J., McGwire, K., Muscheler, R., Nishiizumi, K.,
242 Pasteris, D. R., Rhodes, R. H., & Sowers, T.A. (2016). The WAIS Divide deep ice core WD2014 chronology–Part
243 2: Annual-layer counting (0–31 ka BP). *Climate of the Past*, 12(3), 769-786.
- 244
- 245 WAIS Divide Project Members. (2015). Precise inter-polar phasing of abrupt climate change during the last ice age.
246 *Nature*, 520(7549), 661-665.
- 247
- 248 Jones, T. R., Cuffey, K. M., White, J. W. C., Steig, E. J., Buizert, C., Markle, B. R., McConnell, J. R. and Sigl, M.
249 (2017b). Water isotope diffusion in the WAIS Divide ice core during the Holocene and last glacial, *J. Geophys. Res.*
250 *Earth Surf.*, 122, doi:10.1002/2016JF003938.
- 251
- 252 Johnsen, S. J., H. B. Clausen, K. M. Cuffey, G. Hoffmann, J. Schwander, and T. Creyts (2000), Diffusion of stable
253 isotopes in polar firn and ice: The isotope effect in firn diffusion, in *Physics of Ice Core Records*, edited by T.
254 Hondoh. pp. 121 – 140, Hokkaido Univ. Press, Sapporo.
- 255
- 256 Vinther, B. M., Johnsen, S. J., Andersen, K. K., Clausen, H. B., and Hansen, A. W. (2003). NAO signal recorded in
257 the stable isotopes of Greenland ice cores, *Geophys. Res. Lett.*, 30, 1387, <https://doi.org/10.1029/2002GL016193>.
- 258
- 259 Jouzel, J., Alley, R. B., Cuffey, K. M., Dansgaard, W., Grootes, P. M., Hoffmann, G., Johnsen, S. J., Koster, R. D.,

260 Peel, D., Shuman, C. A., Stievenard, M., Stuiver, M., White, J.W. C., Hammer, C.U., Mayewski, P. A., Peel, D., &
261 Stuiver, M. (1997). Validity of the temperature reconstruction from water isotopes in ice cores. *Journal of*
262 *Geophysical Research*, 102, 26471–26487.

263

264 Küttel, M., Steig, E. J., Ding, Q., Monaghan, A. J., & Battisti, D. S. (2012). Seasonal climate information preserved
265 in West Antarctic ice core water isotopes: relationships to temperature, large-scale circulation, and sea ice. *Climate*
266 *Dynamics*, 39(7-8), 1841-1857.

267

268 Steig, E. J., Ding, Q., White, J. W. C., Kuttel, M., Rupper, S. B., Neumann, T. A., Neff, P. D., Gallant, A. J. E.,
269 Mayewski, P. A., Taylor, K. C., Hoffmann, G., Dixon, D. A., Schoenemann, S. W., Markle, B. R., Fudge, T. J.,
270 Schneider, D. P., Schauer, A. J., Teel, R. P., Vaughn, B. H., Burgener, L., Williams, J., and Korotkikh, E. (2013)
271 Recent climate and ice-sheet changes in West Antarctica compared with the past 2000 years, *Nat. Geosci.*, 6, 372–
272 375.

273

274 Cuffey, K. M., G. D. Clow, E. J. Steig, C. Buizert, T. J. Fudge, M. Koutnik, E. D. Waddington, R. B. Alley, and J.
275 P. Severinghaus (2016), Deglacial temperature history of West Antarctica, *Proc. Natl. Acad. Sci. U.S.A.*,
276 doi:10.1073/pnas.1609132113.

277

278 Markle, B. R., & Steig, E. J.,. "Improving temperature reconstructions from ice-core water-isotope records." *Climate*
279 *of the Past Discussions* (2021): 1-70.

280

281 Huybers, P. (2011). Combined obliquity and precession pacing of late Pleistocene deglaciations. *Nature*, 480(7376),
282 229-232.

283

284 Singarayer, J. S., & Valdes, P. J. (2010). High-latitude climate sensitivity to ice-sheet forcing over the last 120kyr.
285 *Quaternary Science Reviews*, 29(1), 43-55.

286

287 Masson-Delmotte, V., Hou, S., Ekaykin, A., Jouzel, J., Aristarain, A., Bernardo, R. T., Bromwich, D., Cattani, O.,
288 Delmotte, M., Falourd, S., Frezzotti, M., Gallee, H., Genoni, L., Isaksson, E., Landais, A., Helsen, M. M.,
289 Hoffmann, G., Lopez, J., Morgan, V., Motoyama, H., Noone, D., Oerter, H., Petit, J. R., Royer, A., Uemura, R.,
290 Schmidt, G. A., Schlosser, E., Simoes, J. C., Steig, E. J., Stenni, B., Stievenard, M., van den Broeke, M. R., van de
291 Wal, R. S. W., van de Berg, W. J., Vimeux, F., & White, J. W. C. (2008): A review of Antarctic surface snow
292 isotopic composition: observations, atmospheric circulation and isotopic modelling, *J. Climate*, 21, 3359–3387.

293

294 Fortuin, J. P. F., & Oerlemans, J. (1990). Parameterization of the annual surface temperature and mass balance of
295 Antarctica. *Annals of Glaciology*, 14, 78-84.

296

297 Ackert, R. P., Barclay, D. J., Borns, H. W., Calkin, P. E., Kurz, M. D., Fastook, J. L., & Steig, E. J. (1999).
298 Measurements of past ice sheet elevations in interior West Antarctica. *Science*, 286(5438), 276-280.

299

300 Steig, E. J., Fastook, J. L., Zweck, C., Goodwin, I. D., Licht, K. J., White, J. W., & Ackert Jr, R. P. (2001). West
301 Antarctic ice sheet elevation changes. *The West Antarctic Ice Sheet: Behavior and Environment*, 77, 75-90.

302

303 Ackert, R. P., Mukhopadhyay, S., Parizek, B. R., & Borns, H. W. (2007). Ice elevation near the West Antarctic Ice
304 Sheet divide during the last glaciation. *Geophysical Research Letters*, 34(21).
305

306 Pollard, D., Chang, W., Haran, M., Applegate, P., & DeConto, R. (2015). Large ensemble modeling of last deglacial
307 retreat of the West Antarctic Ice Sheet: Comparison of simple and advanced statistical techniques. *Geosci Model*
308 *Devel Disc*, 8, 9925-9963.
309

310 Steig, E. J., Huybers, K., Singh, H. A., Steiger, N. J., Ding, Q. H., Frierson, D. M. W., Popp, T., and White, J. W. C.
311 (2015). Influence of West Antarctic Ice Sheet collapse on Antarctic surface climate, *Geophys. Res. Lett.*, 42, 4862–
312 4868.
313

314 Chiang, J. C., Lee, S. Y., Putnam, A. E., & Wang, X. (2014). South Pacific Split Jet, ITCZ shifts, and atmospheric
315 North–South linkages during abrupt climate changes of the last glacial period. *Earth and Planetary Science Letters*,
316 406, 233-246.
317

318 Inatsu, M., & Hoskins, B. J. (2004). The zonal asymmetry of the Southern Hemisphere winter storm track. *Journal*
319 *of Climate*, 17(24), 4882-4892.
320

321 Ogawa, F., Nakamura, H., Nishii, K., Miyasaka, T., & Kuwano-Yoshida, A. (2016). Importance of midlatitude
322 oceanic frontal zones for the annular mode variability: Interbasin differences in the southern annular mode signature.
323 *Journal of Climate*, 29(17), 6179-6199.
324

325 Nakamura, H., & Shimpo, A. (2004). Seasonal variations in the Southern Hemisphere storm tracks and jet streams
326 as revealed in a reanalysis dataset. *Journal of Climate*, 17(9), 1828-1844.
327

328 Patterson, M., Woollings, T., Bracegirdle, T. J., & Lewis, N. T. (2020). Wintertime Southern Hemisphere jet
329 streams shaped by interaction of transient eddies with Antarctic orography. *Journal of Climate*, 33(24), 10505-
330 10522.
331

332 Goyal, R., Jucker, M., Sen Gupta, A., & England, M. H. (2020). Generation of the Amundsen Sea Low by Antarctic
333 orography. *Geophysical Research Letters*, e2020GL091487.
334

335 Spector, P., Stone, J., Cowdery, S. G., Hall, B., Conway, H., & Bromley, G. (2017). Rapid early-Holocene
336 deglaciation in the Ross Sea, Antarctica. *Geophysical Research Letters*, 44(15), 7817-7825.
337

338 Zhang, W., Yan, H., Dodson, J., Cheng, P., Liu, C., Li, J., Lu, F., Zhou, W., An, Z., 2018. The 9.2 ka event in Asian
339 summer monsoon area: the strongest millennial scale collapse of the monsoon during the Holocene. *Clim. Dyn.* 50,
340 2767–2782. [https:// doi.org/10.1007/s00382-017-3770-2](https://doi.org/10.1007/s00382-017-3770-2).
341

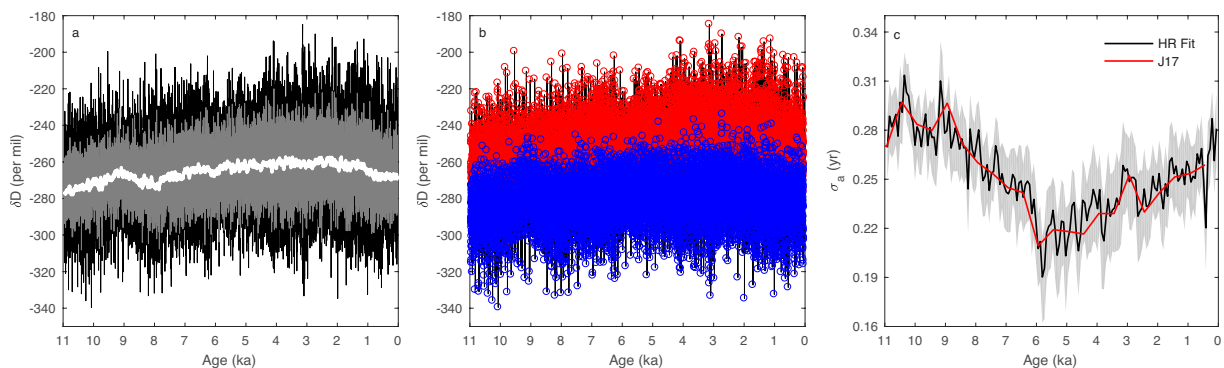
342 Ding, Q., Steig, E. J., Battisti, D. S., & Küttel, M. (2011). Winter warming in West Antarctica caused by central
343 tropical Pacific warming. *Nature Geoscience*, 4(6), 398-403.
344

345 Methods

346 1 Water isotopes

347 Water isotope records from ice cores are proxies primarily for local temperature, dependent on regional atmospheric
348 circulation, that provide a viewpoint into past changes in the hydrologic cycle. Water isotopes are subjected to a
349 smoothing process due to diffusion in the firn column, the uppermost layers of an ice sheet (Johnsen et al. 2000,
350 Cuffey and Steig, 1998). The firn column is 10s of meters thick in most cases, and allows for the movement of water
351 molecules within interconnected vapor pathways for upwards of 100s of years. This smoothing can erase high-
352 frequency climate variations in low accumulation ice core sites and/or sites with firn conditions favorable to
353 diffusion. Moreover, ice core sampling and analysis protocols can further deteriorate high-frequency climate
354 resolution, for example, discrete sampling at 5 cm may bypass important climate information contained at the sub-
355 centimeter scale. Recent advances in continuous flow analysis (CFA) – allowing for millimeter resolution in ice core
356 water isotope records – have generated the highest-resolution paleoclimate records yet recovered (e.g. Jones et al.
357 2017a). The WAIS Divide ice core site (WDC) was conducive to retaining high-frequency climate information due
358 to the high-accumulation rate (Holocene mean = 0.23 m ice eq. yr⁻¹) and cold temperatures, which reduce the effects
359 of firn diffusion (Jones et al. 2017b).

360



361

362 **ED Figure 1 | WDC Water Isotope Data.** **a**, The raw, high-resolution WDC δD water isotope record (grey), the
363 raw 50-yr running mean (white), and the diffusion-corrected signal (black). **b**, The WDC diffusion-corrected δD
364 water-isotope record with extrema picks for summer (red) and winter (blue). **c**, The high-resolution diffusion length
365 record (black; 140 yr windows, 70-yr time steps; 1σ uncertainty bounds in light grey) compared to prior estimates
366 (red; 500-yr windows, 500-yr time steps; Jones et al. 2017b).

367

368 1.1 Water isotope data

369 The WDC water isotope record was analyzed on a CFA system (Jones et al. 2017a) using a Picarro Inc. cavity ring-
370 down spectroscopy (CRDS) instrument, model L2130-i. The raw WDC data was analyzed using permutation
371 entropy (Bandt and Pompe 2002) to automatically identify data anomalies arising from laboratory analysis, which
372 were then corrected by resampling ice over depths of 1035.4 to 1368.2 m (4517 to 6451 yrs) (Garland and Jones et
373 al. 2018). All other Holocene data was previously published (Steig et al., 2013; Jones et al. 2018), and the full data
374 sets are available in an online data repository (White et al. 2020, Jones et al. 2020). The data are reported in delta
375 notation relative to Vienna Standard Mean Ocean Water (VSMOW, δ¹⁸O = δD = 0‰), normalized to Standard Light

376 Antarctic Water (SLAP, $\delta^{18}\text{O} = -55.5\text{‰}$, $\delta\text{D} = -428.0\text{‰}$) scale. WDC is annually dated, with accuracy better than
377 0.5% of the age between 0-12 ka (Sigl et al. 2016).

378

379 **2 Frequency domain analyses**

380 **2.1 Spectral conversion**

381 We use the MultiTaper method fast Fourier transform technique to calculate spectral power densities (Thomson
382 1982, Percival and Walden, 1993) of the measured water isotope time series. Similar to other paleoclimate studies
383 (Jones et al. 2018), we use the ‘pmtm.m’ matlab routine of P. Huybers
384 (<http://www.people.fas.harvard.edu/~phuybers/Mfiles/>). Before spectral analysis, the isotope data are linearly
385 interpolated at a uniform time interval of 0.05 yr.

386

387 **2.2 High-frequency signal attenuation**

388 High-frequency water isotope information in ice cores is attenuated by diffusion in the firn column and deep ice
389 (Johnsen 1977a, Whillans and Grootes 1985, Cuffey and Steig 1998, Johnsen et al. 2000, Gkinis et al. 2014, Jones et
390 al. 2017b). Frequency spectra reveal the amount of signal attenuation as declines in the amplitude of a given
391 frequency through time, relative to lower frequencies. For WDC, the annual signal (1 yr) is indiscernible at ages
392 >14 ka and difficult to interpret >11 ka (Jones et al. 2017b).

393

394 **2.3 Gaussian determination of diffusion lengths**

395 The quantitative effects of diffusion can be represented by the convolution of a Gaussian filter with the original
396 water-isotope signal deposited at the surface and subsequently strained by ice deformation and firn compaction
397 (Johnsen 1977a, Johnsen et al. 2000) (Extended Data Fig. 2). The power density spectrum observed in the ice core
398 record ($P(f)$), after diffusion, is $P(f) = P_o(f) \exp[-(2\pi f \sigma_z)^2]$, where $P_o(f)$ represents the power spectrum of the
399 undiffused signal, f is the frequency $\frac{1}{\lambda}$, λ the signal wavelength, z the depth, and σ_z the diffusion length. Fitting a
400 Gaussian to $P(f)$ using equal log-spaced bins defines a standard deviation, σ_f , with units of 1/meters. The
401 conversion $\sigma_z = \frac{1}{2\pi\sqrt{2}} \cdot \frac{1}{\sigma_f}$ then yields the diffusion length σ_z in units of meters (Jones et al. 2017b). The diffusion
402 length expressed in units of time is $\sigma_t = \frac{\sigma_z}{\lambda_{avg}}$, where λ_{avg} is the mean annual layer thickness (m/yr) at a given depth
403 (Figure 1a). The diffusion length quantifies the statistical vertical displacement of water molecules from their
404 original position in the ice sheet. In this study, equal log-spaced bins for Gaussian fitting and diffusion length
405 estimation reduces window lengths to 140 years (ED Figure 1c), as opposed to our previously published WDC
406 studies that used 500-yr data windows through the interval 0 – 29 ka (Jones et al. 2017b, Jones et al. 2018).

407

408 **2.4 Natural log determination of diffusion length**

409 The σ_f variable can also be determined by using the slope of the linear regression of $\ln(P(f))$ vs. f^2 . This provides a

410 means of estimating diffusion-length uncertainty (Jones et al. 2017b). Here, $\sigma_f = \sqrt{\frac{1}{2 \cdot |(m_{ln})|}}$ where m_{ln} is the slope

411 of the linear regression over the interval from 0.01 cycles²/m² to the value at which systematic noise from the ice
412 core analysis system overwhelms the physical signal. The point where noise dominates appears as a “kink” or
413 “bend” in the decay of ln(P(f)). A maximum and minimum slope is fit within the standard deviation of the linear
414 regression to determine an uncertainty range for σ_f .

415

416 **2.5 Power density diffusion correction and inversion**

417 Diffusion of a water isotope signal in an ice sheet reduces the power of high-frequencies, so $P(f)$ takes the form of
418 quasi-red noise. Given that WDC Holocene spectra show constant power density in the frequencies largely
419 unperturbed by diffusion (periods >4 yrs), we use a white-noise normalization to estimate the original, pre-diffusion
420 power density spectrum. Specifically, we calculate $P_o(f) = P \exp(4\pi^2 f^2 \sigma_t^2)$, where P is the observed power
421 density (per mil²·yr), f the frequency (1/yr), and σ_t the diffusion length (yr).

422

423 We use diffusion correction code developed at the University of Copenhagen by S. Johnsen (Johnsen et al. 2000,
424 Vinther et al. 2003, Hughes et al. 2020), which utilizes the Maximum Entropy Method (MEM) to invert a calculated
425 pre-diffusion power density spectrum $P_o(f)$. The spectrum takes the form of a series of complex numbers $X_R + jX_I$
426 vs. f . From this, the amplitude spectrum A is obtained by $A(f) = \sqrt{X_R^2 + X_I^2}$ and the phase spectrum ϕ is obtained
427 by $\phi(f) = \tan^{-1}\left(\frac{X_I}{X_R}\right)$. The real components of the amplitude and phase spectrums can be used to reconstruct the
428 diffusion corrected water isotope signal $\delta_o(t)$:

$$\delta_o(t) = \sum_{i=1}^N A_i \cos(2\pi f_i t + \phi_i)$$

429 The uncertainty on the diffusion corrected water isotope signal $\delta_o(t)$ is determined using the uncertainty range for
430 diffusion lengths using the natural log determination.

431

432 **2.6 Peak Picking Algorithm**

433 To select extrema (summers and winters) in the diffusion corrected δD signal (Figure 1a, ED Figure 1b), we use the
434 ‘findpeaks’ matlab function. A 50-year boxcar average is applied to the resulting summer and wintertime series to
435 filter out high-frequency noise and distinguish long-term trends (Figure 1c-e).

436

437 **3 Seasonal Preservation Bias of Water Isotopes**

438 The WDC water isotope records of summer, winter, and annual amplitude are influenced by climatic factors,
439 including the seasonal cycle of temperature at the site, which directly influences the water isotope ratios of
440 precipitation, as well changes in as the seasonal cycle of accumulation at the site, which can distort the temperature
441 signal as recorded in the snow pack. Large forcings can drive temperature and accumulation, including insolation,
442 ice sheet elevation, and synoptic climate. Post-depositional processes are important at the annual and seasonal
443 scales, such as attenuation of the signal by diffusion (Cuffey and Steig, 1998, Johnsen et al. 2000). In particular, a
444 differential diffusion effect arising from unequal seasonal distribution of snowfall (Cuffey and Steig, 1998) has
445 largely been ignored in ice core science because records are rarely high enough resolution to detect this process.

446

447 We utilize the Community Firn Model (CFM) (Stevens et al. 2020; Gkinis et al. 2021), a firn-evolution model with
448 coupled firn temperature, firn densification, and water-isotope modules, to test how seasonally weighted
449 accumulation affects the diffusion of the isotope record progressing from surface snow (δD_{snow}), to consolidated
450 snowpack in the firn (δD_{firn}), to solid ice beneath the pore close-off depth (δD_{ice}). The δD_{ice} has been completely
451 diffused after advection through the firn column. We apply the back-diffusion calculation (Johnsen et al. 2000,
452 Vinther et al. 2003; Hughes et al. 2020) to δD_{ice} , to estimate the original δD_{snow} . We then assess how reconstructions
453 of δD_{snow} could be misinterpreted due to different seasonally weighted accumulation (ED Figures 2; 3a,b).

454

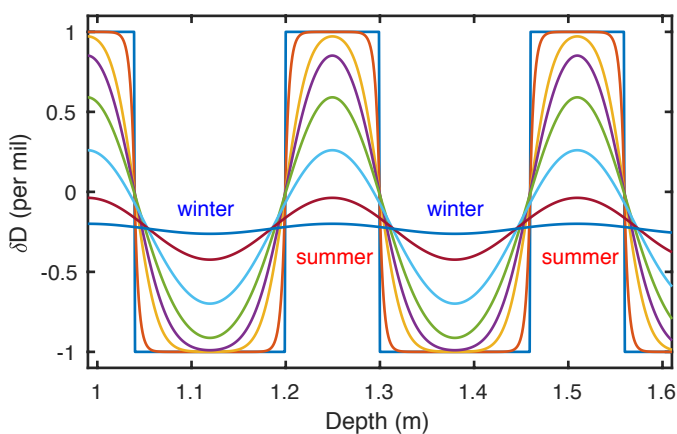
455 We performed five model runs using monthly time steps (ED Table 1). Each run used the same temperature and
456 isotope surface boundary conditions but used different idealized accumulation histories. Each run was for 1014
457 years, which was enough time for the entire firn column to be refreshed (i.e. the firn at the bottom of the model
458 domain, 220 m, was less than 1014 years old). The CFM outputs of interest were the profiles of water isotopes in the
459 firn column at the end of the simulation; these are the model predictions of diffused isotope values after 1000 years
460 of steady-state climate with accumulation variability. We use a seasonal cycle for δD_{snow} based on the mean
461 amplitude in Figure 1b (15.43‰).

462

463 The five accumulation scenarios are all based on the monthly accumulation for WAIS Divide predicted by the
464 regional climate model MAR3.6 (ERA-Interim forced), which spans the period January 1979 to December 2017.
465 The mean accumulation over the entire 39-year period is 0.24745 m ice eq. a⁻¹. The mean \bar{b} and standard deviation
466 σ_b of each month's accumulation are shown in ED Table 1. The five scenarios are as follows. 1) 'constant': the
467 accumulation at each time step is constant (0.0206 m ice eq. month⁻¹; 1/12 the annual mean) for the entire model
468 run. 2) 'cycle': accumulation for each month is the MAR mean accumulation for that month, as shown in ED Table
469 1's 'mean' column. This annual cycle is repeated for the 1014-year duration of the model run. 3) 'noise': using the
470 'cycle' time series, we add noise to each time step by drawing a random number from a normal distribution with
471 zero mean and standard deviation equal to that month's σ value in ED Table 1. 4) 'random': for each month, a
472 random number is selected from the normal distribution with that month's mean and σ as in ED Table 1. 5) 'loop':
473 the entire 39-year MAR accumulation time series is repeated over and over again. The 'noise' and 'random' were
474 adjusted so that the minimum accumulation rate for any one-month was 0.01 m ice eq. a⁻¹ and so that the mean
475 accumulation of the time series was the same as the mean 1979-2017 accumulation from MAR. For the temperature
476 boundary condition, we used each month's mean 1979-2017 2 m temperature predicted by MAR to create an annual
477 temperature cycle. We repeated this 12-month time series for the duration of the model runs. This method ensures
478 that the model runs, which are designed to test effects of accumulation seasonality, are not affected by interannual
479 temperature variability, while also providing a reasonable estimate of the annual temperature cycle, which affects
480 the rate of isotope diffusion in the upper firn. The annual temperature cycle and the repeated annual-isotopic cycle
481 we used are shown in ED Table 1.

482

483 ED Figure 3 shows the results for the ‘constant’ distribution of monthly snowfall (i.e. each month receives 1/12 of
 484 the modern annual snowfall of 0.247 m ice eq. yr⁻¹) and the ‘cycle’ distribution specific to WDC predicted by the
 485 regional climate model MAR (Modèle Atmosphérique Régional, Agosta et al. 2019). The MAR scenario has about
 486 1.6x as much snow in winter (Oct-Mar) as summer (Apr-Sep). The diffusion-correction technique accurately
 487 reconstructs δD_{snow} for summer and winter in the ‘constant’ snowfall scenario, but underestimates summer values in
 488 the MAR ‘cycle’ scenario by $\sim 2.6\text{‰}$, which is 11% of the full range of the observed WDC summer water isotope
 489 values. With more seasonal accumulation, winter values are overestimated by only $\sim 0.6\text{‰}$, about 3% of the full
 490 winter range. A full reversal from MAR to a counterfactual scenario in which summer has 1.6x as much summer
 491 snow as winter, would lead to summer and winter values that could vary by up to 3.2‰. The ‘noise’, ‘random’, and
 492 ‘loop’ runs produce results for the reconstructed δD_{snow} within 0.3‰. These CFM experiments demonstrate that
 493 centennial trends in the summer and winter water isotopes on the order of a few per mil could arise from large
 494 changes in seasonal accumulation weighting, while multi-millennial trends $\gg 3.2\text{‰}$ are unlikely to be caused by
 495 seasonal accumulation and can therefore be interpreted as climate signals of a different origin.



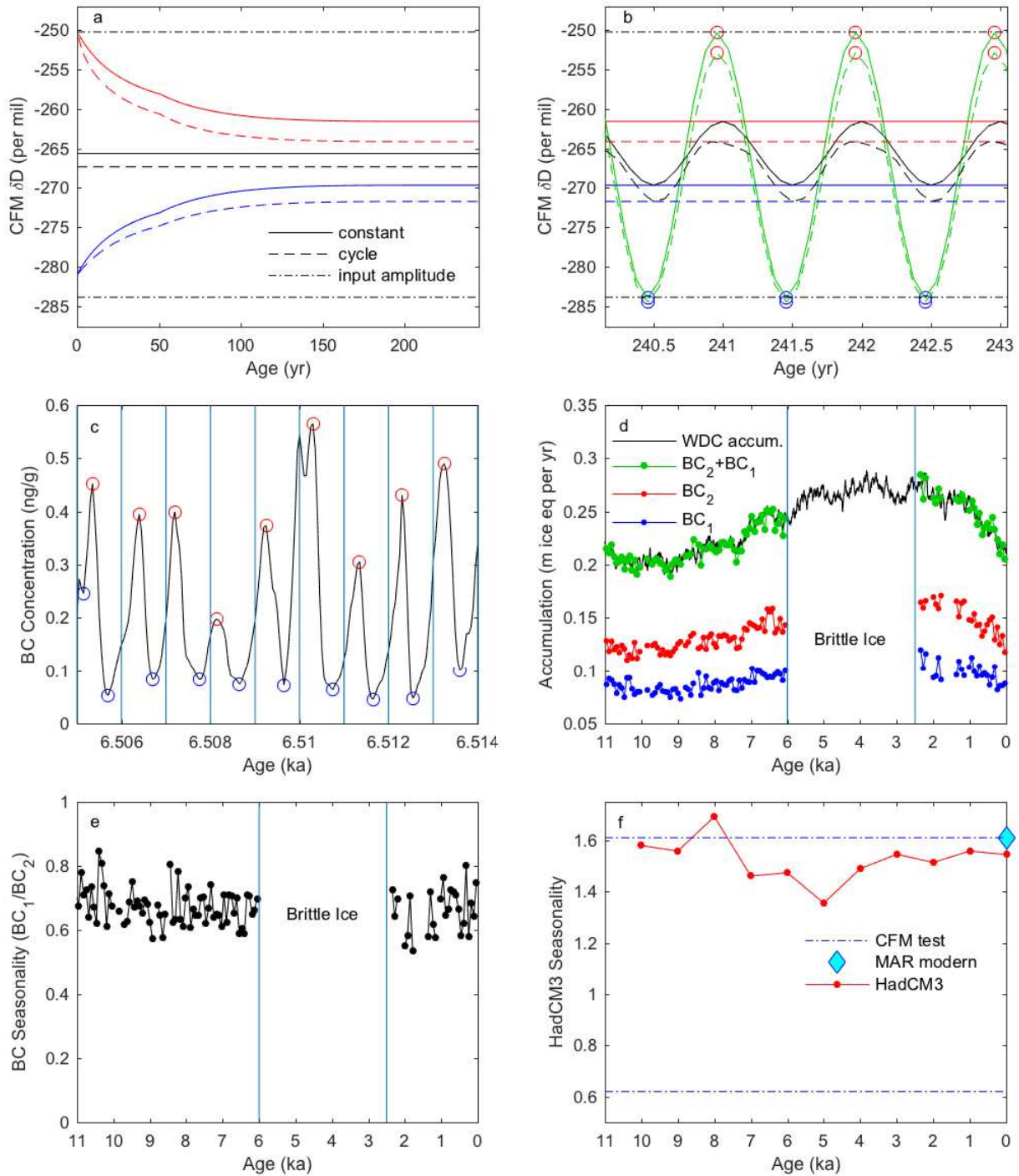
496
 497 **ED Figure 2 | Community Firn Model. a,** Square wave analysis of water isotope diffusion using MAR-
 498 accumulation and temperature weighting for WDC. With progressive diffusion, the summer signal is attenuated
 499 faster (due to lower accumulation than winter), while the annual mean does not change.

500 **ED Table 1:** Mean \bar{b} and standard deviation σ_b of each month's accumulation rate and monthly mean temperature
 501 at WAIS Divide for 1979 to 2017 predicted by MAR and the isotope values used for each month during the CFM
 502 simulations.

Month	\bar{b} (m ice eq. a ⁻¹)	σ_b m ice eq. a ⁻¹	T (°C)	δD (per mil)
1	0.139	0.088	-17.5	-250.22
2	0.169	0.072	-24.9	-252.48
3	0.267	0.010	-31.5	-258.64
4	0.293	0.121	-34.6	-267.05
5	0.345	0.137	-34.9	-275.46
6	0.311	0.136	-36.2	-281.61
7	0.310	0.111	-38.1	-283.87
8	0.298	0.116	-38.6	-281.61
9	0.275	0.112	-37.1	-275.46
10	0.271	0.136	-31.6	-267.05
11	0.164	0.079	-23.8	-258.64
12	0.128	0.071	-17.3	-252.48

503
 504
 505 To determine if there were significant changes in seasonal snowfall across the Holocene, we utilize the only
 506 available age-scale-independent impurity with a relatively well-understood seasonal cycle: black carbon (BC)
 507 concentrations. BC data is available from 0 to 2.5 ka and 6 to 11 ka (Extended Data Figure 4), with no data within
 508 the brittle ice zone. The BC concentrations at WDC are dominated by seasonal fire regimes in South America,
 509 notably the east Amazon, with maximum BC occurring in fall and minimum BC occurring in spring (Arienzo et al.
 510 2017; ED Figure 3c). For a given impurity (I) like BC, the difference in depth, D , between seasonal maximum (f_{\max})
 511 and minimum (f_{\min}) markers can be determined. We split any given year into two parts, the first in which f rises and
 512 the second in which f falls. Here, $I_1 = D(f_{\min(i)}) - D(f_{\max(i)})$ and $I_2 = D(f_{\max(i+1)}) - D(f_{\min(i)})$ represent the two portions of
 513 the seasonal cycle of year i . For BC, I_1 and I_2 (which we will term BC_1 and BC_2 , for simplicity) delineate seasonal
 514 depth intervals for some portion of winter and summer, respectively. The duration of BC_2 is longer than BC_1 due to
 515 the seasonal cycle of BC at the source (Arienzo et al. 2017), thus $BC_1/BC_2 < 1$ (ED Figure 3e). The BC_1/BC_2 ratio
 516 can change with time due to variability at the source, changes in atmospheric transport, or because of seasonal snow
 517 deposition. We observe little change in BC_1/BC_2 resembling the multi-millennial trends seen in WDC summers and
 518 winters (ED Figure 3d,e). Unless there are competing and exactly compensating effects in seasonality (i.e. the
 519 source change exactly cancels the depositional and transport change, or other unlikely scenarios), the changes in
 520 WDC seasonal snowfall are not of sufficient magnitude (also supported by HadCM3, ED Figure 3f) to affect our
 521 multi-millennial climate interpretations of annually resolved water isotopes. Further, it is very likely that the CFA
 522 tests we performed are an extremely conservative estimate of how the seasonality of snowfall can impact
 523 interpretations of summer and winter δD .

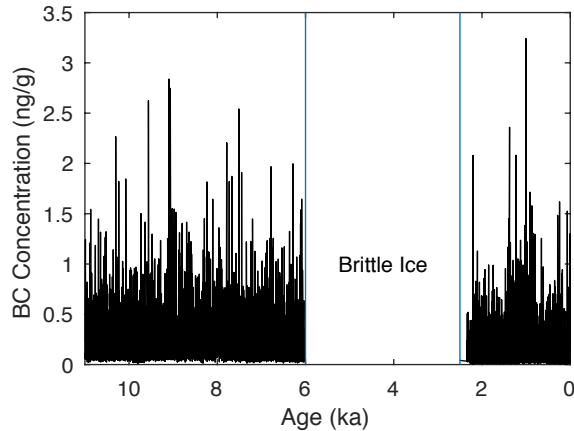
524



525

526 **ED Figure 3 | Seasonally weighted accumulation.** *a*, The diffusion envelope of CFM output data (50-yr avg.),
 527 based on an input sine wave with $f=1\text{yr}^{-1}$ and amplitude=15.43‰. The original amplitude of the signal (based on
 528 the dotted dashed lines) decreases as time passes due to downward advection of the firn, as shown by the decay of
 529 the maximum (red) and minimum (blue) lines, while the mean values of the 'constant' and 'cycle' scenarios do not
 530 change, dependent on the seasonal weighting of snowfall. *b*, Diffused CFM output data from beneath the pore close-
 531 off depth (>200 yr) (black lines), with diffusion corrected data shown with green lines. Red circles are the annual
 532 maximum value, and blue circles the annual minimum, selected using the same algorithm as Figure 1a. *c*, A zoom of
 533 black carbon concentrations at ~6.5 ka. The maxima (red circles) and minima (blue circles) can be used to separate

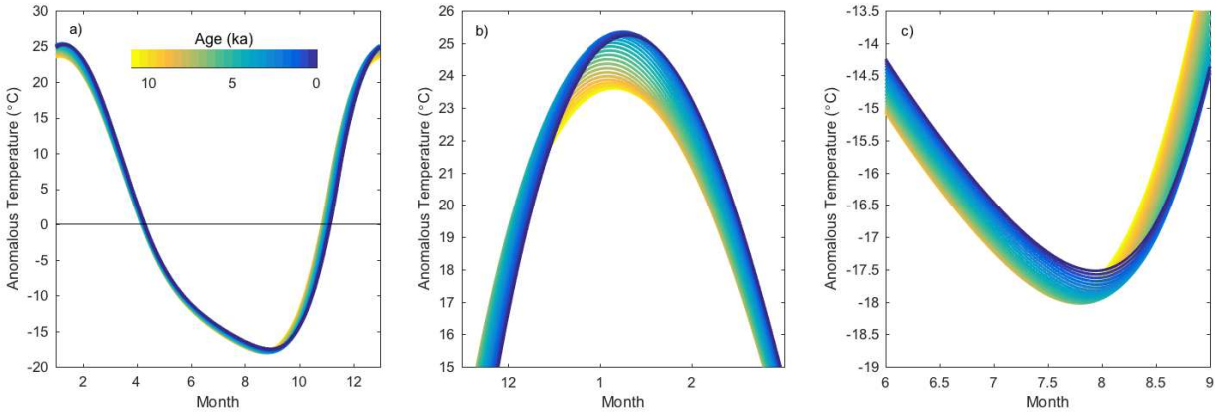
534 *approximate depth intervals corresponding to winter (BC₁) and summer (BC₂); vertical blue lines correspond to*
 535 *nominal January 1, as defined by the peak of nssS/Na (Sigl et al. 2016). d, The 140-yr averages for BC₁ (blue) and*
 536 *BC₂ (red). The black line is WDC annual accumulation (Fudge et al. 2016); green circles are BC₁ + BC₂, which*
 537 *should equal annual accumulation. e, Black carbon seasonality BC₁/ BC₂ (black), based on (d). f, Accumulation*
 538 *seasonality for HadCM3 seasonal snowfall (red line) compared to the range of seasonality tested using the CFM*
 539 *(dashed blue lines) and modern MAR seasonality (blue diamond).*
 540



541
 542 **ED Figure 4 | Black Carbon.** *Annually resolved black carbon data (Bisiaux et al. 2012, Arienzo et al. 2017). The*
 543 *missing data is from the brittle ice zone, where it was not possible to measure black carbon using continuous flow*
 544 *techniques.*
 545

546 **4 Seasonal Energy Balance Model**

547 We use a relatively simple energy balance model to calculate expected changes in seasonal and monthly surface
 548 temperature (ED Figure 5). Our model is a global, zonal mean energy balance model. The model accounts for TOA
 549 insolation, a temperature-dependent long-wave emission to space, a simple temperature dependent albedo in which
 550 sufficiently cold surfaces are bright simulating snow and ice, and horizontal atmospheric heat transport which is
 551 modeled as the diffusion of near-surface moist static energy (MSE) (Hwang and Frierson 2010, Roe et al. 2015,
 552 Siler et al. 2018). The model has a 2-degree spatial resolution, a single surface and single atmospheric layer, and the
 553 surface heat capacity is based on the relative fraction of land and ocean surface in the zonal mean. Heat exchange
 554 between the surface and atmosphere layers is modeled as the difference in blackbody radiation from each layer in
 555 addition to sensible and latent heat exchange proportional to the temperature and specific humidity difference of
 556 each layer (assuming a constant relative humidity of 80%), following bulk aerodynamic formulae. We calculate the
 557 annual TOA insolation cycle at every latitude in 500-yr time slices from present to 11 ka. For each time slice the
 558 model is run at a 2-hour time resolution for 30 model years to reach equilibrium.
 559



560

561 **ED Figure 5 | MEBM seasonal surface temperature.** *a*, Modeled seasonal surface temperature cycle at 80°S,
 562 colored by age. *b*, *c*, Zoom in of modeled summer and winter temperature.

563

564

565

566

567

568

569

570

571

572

573

574

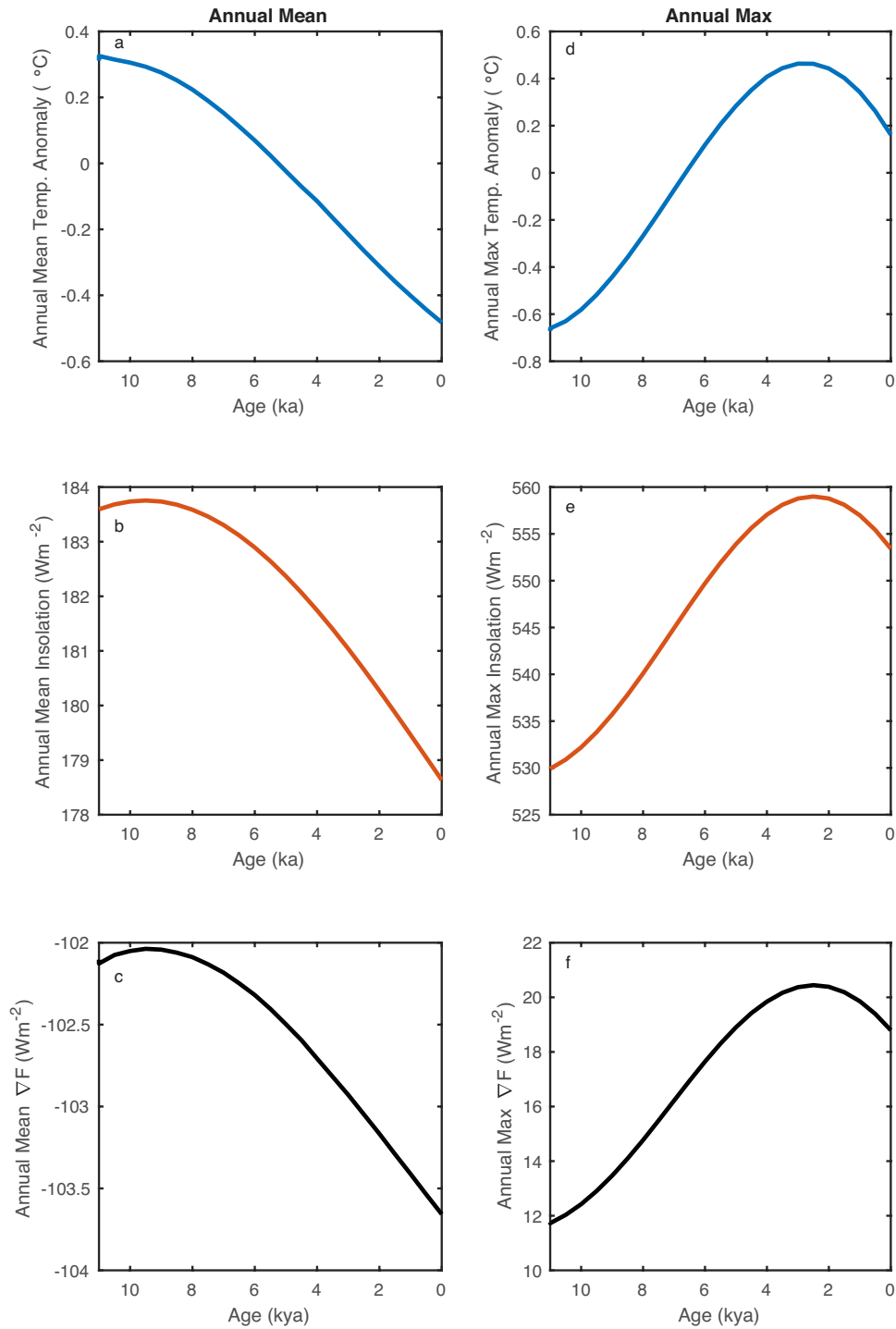
575

576

577

578

How important is local insolation in driving the heating, which in turn drives the changes in maximum summer temperature over the Holocene? While heat transport from lower latitudes can connect changes in insolation at distal locations to the WDC site, local heating is by far the dominant factor. The temporal pattern of peak summer insolation across latitudes is shown in Figure 2f, with the WDC site latitude shown as the thick black line. The pattern of maximum summer temperature modeled by the MEBM is most closely correlated to the local peak insolation, rather than the pattern of insolation at lower latitudes. In ED Figure 6 we examine changes in heat transport along with that of local insolation. We compare the temporal evolution of annual mean and peak summer heat divergence by the atmosphere (∇F) at the WDC site to the annual mean and summer maximum site temperature and insolation. While Holocene changes in ∇F at the WDC site are correlated with insolation forcing, the magnitude of changes in maximum direct insolation are much larger than those in atmospheric heat divergence. Further the Holocene changes in summertime heat divergence are of the wrong sign to cause net heating at the WDC site (positive divergence is an export of heat by the atmosphere from the site). Note that in the annual mean heat transport is convergent in the Antarctic, however at the peak of summer it is divergent, owing to the intense incoming insolation but low longwave emission from low surface temperatures.



579
 580 **ED Figure 6 | MEBM Results.** *a-c*, Annual mean temperature anomaly (blue), insolation (red), and heat
 581 divergence (black), respectively at 80°S from the MEBM. *d-f*, Annual maximum temperature anomaly (blue),
 582 insolation (red), and heat divergence (black), respectively at 80°S from the MEBM. Note the sign of heat
 583 divergence; negative values correspond to heat convergence at the site.

584 **5 HadCM3 model simulations**

585 **5.1 Model setup**

586 We use the fully coupled ocean-atmosphere model HadCM3 (Gordon et al. 2000, Valdes et al. 2017). The exact
587 model version is HadCM3BM2.1. This model has been shown to simulate the climate in the tropical Pacific very
588 well, including in its response to glacial forcing (DiNezio and Tierney 2013). We simulate the climate over the last
589 11 ka in a series of snapshots run every 1 kyr (Singarayer and Valdes 2010). For each snapshot, we prescribe
590 changes to a number of boundary conditions: the orbital forcing (Berger and Loutre 1991), greenhouse gas (GHG)
591 concentration (Spahni et al. 2005, Loulergue et al. 2008), ice sheet topography, and sea level (Argus et al. 2014,
592 Peltier et al. 2015, Tarasov and Peltier, 2002; Tarasov et al. 2012, Briggs et al. 2014, Tarasov et al. 2014, Abe-Ouchi
593 et al. 2013). In the main text we use three sets of simulations: 1) only orbital forcing changes (ORBIT), all other
594 boundary conditions remain as for the pre-industrial 2) orbital/GHG forcing with the GLAC1D ice sheet elevation
595 history, and 3) orbital/GHG forcing with the ICE-6G ice sheet elevation history. Elevation histories are shown in
596 Figure 4a: GLAC1D is 96 meters higher at 11ka compared to present, and ICE-6G is 222 meters higher. All
597 snapshot simulations are run for at least 500 years with analysis made on the final 100 years of each simulation. We
598 use further simulations of 10ka to more clearly decompose the role of different forcings. These are described in the
599 following sections.

600

601 **5.2 Seasonality of Accumulation**

602 HadCM3 shows a negligible change in the seasonality of accumulation (ED Figure 3f), with 1.5 times as much snow
603 falling in winter than in summer throughout the Holocene. There is about 10% less precipitation during the early
604 part of the Holocene in both winter and summer. Small changes in the weighting for winter and summer
605 precipitation are evident. In winter, the total snowfall ranges from 30% at 10 ka to 28% in the modern. The change
606 in summer snowfall is less than 1%. Overall, HadCM3 shows a negligible change in the accumulation with 1.5 times
607 as much snow falling in winter than in summer throughout the Holocene.

608

609 **5.3 Summer Climate**

610 To elucidate forcing mechanisms compared with the Moist Energy Balance Model (MEBM), we examine the zonal
611 mean at 80°S in a set of 10 ka simulation compared to a pre-industrial simulation in HadCM3. These simulations are
612 ‘10ka ORBIT’; two runs with only 10 ka ice sheets and all other settings as for the pre-industrial, including ‘10 ka
613 ice sheet only with GLAC1D’ and ‘10ka ice sheet only with ICE-6G’; and two runs with all 10 ka forcing, including
614 ‘10ka all forcings with GLAC1D’, and ‘10ka all forcings with ICE-6G’. In ‘10ka ORBIT’ there is a cooling in
615 summer that is predominantly caused by the large reduction in shortwave radiation at the surface (SW_d), caused by
616 the reduced shortwave radiation at the TOA. SW_d is not the only reduced surface flux: the downward longwave
617 radiation (LW_d) is also reduced, likely due to the cooling of the atmospheric column. Interestingly there is an
618 increased sensible heat flux (SH) indicating that the atmosphere and surface do not equally cool; one cause of this is
619 the increased meridional heat convergence (∇F).

620

621 The simulations ‘10ka ice sheet only with GLAC1D’ and ‘10ka ice sheet only with ICE-6G’ both show a summer
622 time cooling in response to the imposed ice sheet. The largest contributor to this is LW_d . The decrease in the
623 temperature is not the same in the two simulations: the cooling in ‘10ka ice sheet only with ICE-6G’ is much larger,
624 attributable to the much larger reduction in LW_d than in ‘10ka ice sheet only with GLAC1D’. Both simulations also
625 show an increase in SW_d , which counteracts the reduced LW_d to some extent. Both the change in LW_d and SW_d can
626 be explained by the presence of the ice sheet. The larger ice sheet reduces the depth of the atmospheric column,
627 reducing the amount of SW radiation absorbed between the TOA and the surface; a reduced depth of the atmosphere
628 will also tend to cool the column average temperature, thus reducing LW_d . Remote processes can also change the
629 atmospheric temperature, and we see that both ice sheet reconstructions cause an increase in ∇F . This increase is
630 larger in ‘10ka ice sheet only with GLAC1D’. Because ∇F will tend to warm the atmospheric column it could
631 explain why the reduction in LW_d is smaller in ‘10ka ice sheet only with GLAC1D’ than ‘10ka ice sheet only with
632 ICE-6G’.

633
634 With all 10k forcings we find a cooling that is caused by both LW_d and SW_d . The decrease in SW_d is similar in ‘10ka
635 all forcings with GLAC1D’ and ‘10ka all forcings with ICE-6G’ and slightly smaller than in ‘10ka ORBIT’, likely
636 due to the decreased absorption due to the thinner atmospheric column. The decrease in LW_d in ‘10ka all forcings
637 with GLAC1D’ and ‘10ka all forcings with ICE-6G’ is larger than that in ‘10ka ORBIT’, ‘10ka ice sheet only with
638 GLAC1D’, and ‘10ka ice sheet only with ICE-6G’; it is also somewhat larger than the linear combination of the
639 change in ‘orbit only’ and ‘10k ice sheet only with GLAC1D/ICE-6G’. This indicates the importance of feedbacks
640 in the atmosphere. These could be remote feedbacks, there is an increase in ∇F in both simulations, or local
641 feedbacks related to the amount of water vapor in the atmosphere.

642
643 The description of changes in the zonal mean in the 10 ka simulations compared to pre-industrial holds for the entire
644 Holocene. With only changes to the orbital forcing there is a reduction in SW_d and LW_d of roughly the same
645 magnitude. With full forcing (including ice sheets), the reduction in LW_d is roughly three times the reduction in SW_d .
646 If an energy budget over the WDC site (79.467°S 112.085°W) is considered, a similar description as for the zonal
647 mean applies. The magnitude of the forcings are changed, but reduced SW_d still cools the surface, amplified by a
648 LW_d feedback which is dependent on the size of the ice sheet. The ICE-6G simulation cools in summer by an
649 unrealistic amount at 11-8ka, possibly driven by unrealistic winter cooling when the ice sheet is large, but as we
650 have shown (Figure 4a-c), the ICE-6G reconstruction is not consistent with elevation changes constrained by
651 summer isotopes.

652 653 **5.4 Winter Climate**

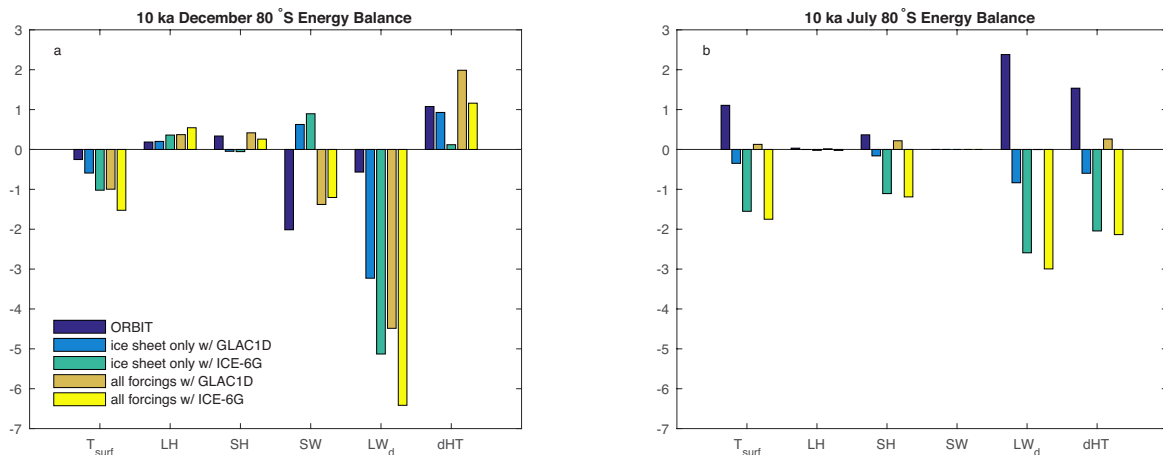
654 During winter the balance of terms is quite different: SW_d is no longer a factor as the sun is below the horizon. Given
655 that there is no change in SW_d in ‘10ka ORBIT’ during winter, we might expect that there would be no change in the
656 surface temperature, however, there is a warming. Examining the energy balance terms we find that this warming is
657 caused by an increase in LW_d . Since there is no local cause for LW_d to change we must look to a remote cause of

658 atmospheric warming. We find that there is an increase in ∇F in ‘10ka ORBIT’, this would act to warm the
 659 atmospheric temperature, in turn increasing LW_d , and also SH . With an ice sheet imposed we find that the surface
 660 temperature cools. This again can be explained by a change in ∇F : in both ‘10ka ice sheet only with GLAC1D’ and
 661 ‘10ka ice sheet only with ICE-6G’ there is a reduction in ∇F which would cool the atmosphere and thus reduce LW_d
 662 and SH . When all 10k forcings are introduced we find that there is a smaller change in the temperature than when
 663 the ice sheet alone was imposed. The LW_d and a change in ∇F can again explain this temperature change. In ‘10ka
 664 all forcings with GLAC1D’ we find no change in ∇F , no change in LW_d and no change in the surface temperature.
 665 This suggests that the increase in ∇F from orbital forcing is almost perfectly balanced by the change in ∇F from the
 666 ice sheet configuration.

667

668 We must acknowledge that the processes that control the heat transport over Antarctica are complicated and that
 669 HadCM3 may not be able to simulate them perfectly. However our simulations do indicate that during winter the
 670 heat transport is crucially important to the atmospheric and surface temperature and more generally that remote
 671 processes can alter the surface temperature quite dramatically. In experiment ‘10ka ORBIT’ and in the MEBM we
 672 find significant changes to the temperature despite no local forcing.

673



674

675 **ED Figure 7 | 80°S Energy Balance at 10 ka.** Bar charts of HadCM3 energy balance terms at 10 ka for **a**,
 676 December (summer) and **b**, July (winter), including model runs for ‘orbit only’ (purple, ORBIT), ‘ice sheet only’
 677 (blue, GLAC1D; green, ICE-6G), and ‘all forcings’ (orange, GLAC1D; yellow, ICE-6G). Positive values all
 678 indicate a surface or atmospheric warming. Variables include surface temperature (T_{surf} in °K), latent heat (LH in
 679 Wm^{-2}), sensible heat (SH in Wm^{-2}), shortwave radiation (SW in Wm^{-2}), downward LW radiation (LW_d in Wm^{-2}),
 680 and change in heat transport (∇F in $10^7 W$).

681 **References**

- 682 Cuffey, K. M., & Steig, E. J. (1998). Isotopic diffusion in polar firn: implications for interpretation of seasonal
683 climate parameters in ice-core records, with emphasis on central Greenland. *Journal of Glaciology*, 44(147), 273-
684 284.
- 685
- 686 Bandt, C., & Pompe, B. (2002). Permutation entropy: a natural complexity measure for time series. *Physical review*
687 *letters*, 88(17), 174102.
- 688
- 689 Garland, J., Jones, T. R., Neuder, M., Morris, V., White, J. W., & Bradley, E. (2018). Anomaly detection in
690 paleoclimate records using permutation entropy. *Entropy*, 20(12), 931.
- 691
- 692 Thomson, D. J. Spectrum estimation and harmonic analysis. *Proceedings of the IEEE* 70, 1055–1096 (1982).
- 693
- 694 Percival, D. B., & Walden, A. T. *Spectral Analysis for Physical Applications*, 583 pp., Cambridge Univ. Press, New
695 York (1993).
- 696
- 697 Johnsen, S. J., Stable isotope homogenization of polar firn and ice, *Proceedings of Symposium on Isotopes and*
698 *Impurities in Snow and Ice, IAHS-AISH Publ.* 118, 210–219 (1977a).
- 699
- 700 Whillans, I. M. & Grootes, P. M. Isotopic diffusion in cold snow and firn. *Journal of Geophysical Research* 90,
701 3910–3918 (1985).
- 702
- 703 Gkinis, V., Simonsen, S. B., Buchardt, S. L., White, J. W. C. & Vinther, B. M. Water isotope diffusion rates from
704 the NorthGRIP ice core for the last 16,000 years – glaciological and paleoclimatic implications. *Earth and Planetary*
705 *Science Letters* 405, 132–141 (2014).
- 706
- 707 Hughes, A. G., Jones, T. R., Vinther, B. M., Gkinis, V., Stevens, C. M., Morris, V., Vaughn, B. H., Holme, C.,
708 Markle, B. R. & White, J.W.C. (2020). High-frequency climate variability in the Holocene from a coastal-dome ice
709 core in east-central Greenland. *Climate of the Past*, 16(4), pp.1369-1386.
- 710
- 711 Stevens, C. M., Verjans, V., Lundin, J., Kahle, E. C., Horlings, A. N., Horlings, B. I., & Waddington, E. D. (2020).
712 The Community Firn Model (CFM) v1. 0. *Geoscientific Model Development*, 13(9), 4355-4377.
713 <https://doi.org/10.1029/2002GL016193>.
- 714
- 715 Gkinis, V., Holme, C., Kahle, E. C., Stevens, M. C., Steig, E. J., & Vinther, B. M. (2021). Numerical experiments
716 on firn isotope diffusion with the Community Firn Model. *Journal of Glaciology*, 1-23.
- 717
- 718 Agosta, C., Amory, C., Kittel, C., Orsi, A., Favier, V., Gallée, H., van den Broeke, M. R., Lenaerts, J. T. M., van
719 Wessem, J. M., van de Berg, W. J., and Fettweis, X.: Estimation of the Antarctic surface mass balance using the
720 regional climate model MAR (1979–2015) and identification of dominant processes, *The Cryosphere*, 13, 281–296,
721 <https://doi.org/10.5194/tc-13-281-2019>, 2019.
- 722
- 723 Arienzo, M. M., McConnell, J. R., Murphy, L. N., Chellman, N., Das, S., Kipfstuhl, S., & Mulvaney, R. (2017).

724 Holocene black carbon in Antarctica paralleled Southern Hemisphere climate. *Journal of Geophysical Research:*
725 *Atmospheres*, 122(13), 6713-6728.

726

727 Fudge, T. J., Markle, B. R., Cuffey, K. M., Buizert, C., Taylor, K. C., Steig, E. J., Waddington, E. D., Conway, H.,
728 and Koutnik, M.: Variable relationship between accumulation and temperature in West Antarctica for the past 31
729 000 years, *Geophys. Res. Lett.*, 43, 3795–3803, <https://doi.org/10.1002/2016GL068356>, 2016.

730

731 Bisiaux, M. M., Edwards, R., McConnell, J. R., Curran, M. A. J., Van Ommen, T. D., Smith, A. M., Neumann, T.
732 A., Pasteris, D. R., Penner, J.E. & Taylor, K. (2012). Changes in black carbon deposition to Antarctica from two
733 high-resolution ice core records, 1850–2000 AD. *Atmospheric Chemistry and Physics*, 12(9), pp.4107-4115.

734

735 Hwang, Y. T., & Frierson, D. M. (2010). Increasing atmospheric poleward energy transport with global warming.
736 *Geophysical Research Letters*, 37(24).

737

738 Roe, G. H., Feldl, N., Armour, K. C., Hwang, Y. T., & Frierson, D. M. (2015). The remote impacts of climate
739 feedbacks on regional climate predictability. *Nature Geoscience*, 8(2), 135-139.

740

741 Siler, N., Roe, G. H., & Armour, K. C. (2018). Insights into the zonal-mean response of the hydrologic cycle to
742 global warming from a diffusive energy balance model. *Journal of Climate*, 31(18), 7481-7493.

743

744 Gordon, C., Cooper, C., Senior, C. A., Banks, H., Gregory, J. M., Johns, T. C., Mitchell, J. F. & Wood, R. A.
745 (2000). The simulation of SST, sea ice extents and ocean heat transports in a version of the Hadley Centre coupled
746 model without flux adjustments. *Climate dynamics*, 16(2), pp.147-168.

747

748 Valdes, P. J., Armstrong, E., Badger, M. P. S., Bradshaw, C. D., Bragg, F., Crucifix, M., Davies-Barnard, T., Day, J.
749 J., Farnsworth, A., Gordon, C., Hopcroft, P. O., Kennedy, A. T., Lord, N. S., Lunt, D. J., Marzocchi, A., Parry, L.
750 M., Pope, V., Roberts, W. H. G., Stone, E. J., Tourte, G. J. L., & Williams, J. H. T.: The BRIDGE HadCM3 family
751 of climate models: HadCM3@Bristol v1.0, *Geosci. Model Dev.*, 10, 3715–3743, [https://doi.org/10.5194/gmd-10-](https://doi.org/10.5194/gmd-10-3715-2017)
752 3715-2017, 2017.

753

754 DiNezio, P. N. & Tierney, J. E. (2013). The effect of sea level on glacial Indo-Pacific climate. *Nature Geoscience* 6,
755 485–491.

756

757 Berger, A. & Loutre, M. F. Insolation values for the climate of the last 10 million years. *Quaternary Science*
758 *Reviews* 10, 297–317 (1991).

759

760 Spahni, R., Chappellaz, J., Stocker, T. F., Loulergue, L., Hausammann, G., Kawamura, K., Flückiger, J., Schwander,
761 J., Raynaud, D., Masson-Delmotte, V. & Jouzel, J. (2005). Atmospheric methane and nitrous oxide of the late
762 Pleistocene from Antarctic ice cores. *Science*, 310(5752), pp.1317-1321.

763

764 Loulergue, L., Schilt, A., Spahni, R., Masson-Delmotte, V., Blunier, T., Lemieux, B., Barnola, J. M., Raynaud, D.,
765 Stocker, T. F. & Chappellaz, J. (2008). Orbital and millennial-scale features of atmospheric CH₄ over the past
766 800,000 years. *Nature*, 453(7193), pp.383-386.

767
768 Argus, D. F., Peltier, W. R., Drummond, R., & Moore, A. W. (2014). The Antarctica component of postglacial
769 rebound model ICE-6G_C (VM5a) based on GPS positioning, exposure age dating of ice thicknesses, and relative
770 sea level histories. *Geophysical Journal International*, 198(1), 537-563.
771
772 Peltier, W. R., Argus, D. F., & Drummond, R. (2015). Space geodesy constrains ice age terminal deglaciation: The
773 global ICE-6G_C (VM5a) model. *Journal of Geophysical Research: Solid Earth*, 120(1), 450-487.
774
775 Tarasov, L., & Richard Peltier, W. (2002). Greenland glacial history and local geodynamic consequences.
776 *Geophysical Journal International*, 150(1), 198-229.
777
778 Tarasov, L., Dyke, A. S., Neal, R. M., & Peltier, W. R. (2012). A data-calibrated distribution of deglacial
779 chronologies for the North American ice complex from glaciological modeling. *Earth and Planetary Science*
780 *Letters*, 315, 30-40.
781
782 Briggs, R. D., Pollard, D., & Tarasov, L. (2014). A data-constrained large ensemble analysis of Antarctic evolution
783 since the Eemian. *Quaternary science reviews*, 103, 91-115.
784
785 Tarasov, L., Hughes, A., Gyllencreutz, R., Lohne, O. S., Mangerud, J., & Svendsen, J. I. (2014, May). The global
786 GLAC-1c deglaciation chronology, meltwater pulse 1-a, and a question of missing ice. In IGS Symposium:
787 Contribution of Glaciers and Ice Sheets to Sea-Level Change, Chamonix, France (pp. 26-30).
788
789 Abe-Ouchi, A., Saito, F., Kawamura, K., Raymo, M. E., Okuno, J. I., Takahashi, K., & Blatter, H. (2013).
790 Insolation-driven 100,000-year glacial cycles and hysteresis of ice-sheet volume. *Nature*, 500(7461), 190-193.
791

792 **Acknowledgements**

793 This work was supported by US National Science Foundation (NSF) grants 0537593, 0537661, 0537930, 0539232,
794 1043092, 1043167, 1043518, and 1142166. Field and logistical activities were managed by the WAIS Divide
795 Science Coordination Office at the Desert Research Institute, Reno, NE, USA and the University of New
796 Hampshire, USA (NSF grants 0230396, 0440817, 0944266, and 0944348). The National Science Foundation
797 Division of Polar Programs funded the Ice Drilling Program Office (IDPO), the Ice Drilling Design and Operations
798 (IDDO) group, the National Ice Core Laboratory (NICL), the Antarctic Support Contractor, and the 109th New York
799 Air National Guard. W.H.G.R. was funded by a Leverhulme Trust Research Project Grant. HadCM3 simulations
800 were carried out using the computational facilities of the Advanced Computing Research Centre, University of
801 Bristol - <http://www.bris.ac.uk/acrc/> and Oswald, University of Northumbria. We thank Cécile Agosta for providing
802 the MAR outputs. We thank the Stable Isotope Lab at INSTAAR for their expertise in helping to measure the water
803 isotope data sets used in this study, especially Valerie Morris and Bruce Vaughn.

804

805 **Author Contributions**

806 T.R.J. designed the project. T.R.J., B.R.M., W.H.G.R., K.M.C., and E.J.S. led the writing of the paper. T.R.J. and
807 J.W.C.W. contributed high-resolution water isotope measurements. W.H.G.R. and P.J.V. conducted HadCM3
808 simulations. B.R.M. conducted MEBM simulations. C.M.S. conducted CFM simulations. T.R.J., K.M.C., and
809 B.M.V. developed the diffusion-correction calculations, with assistance from A.G.H., C.A.B., and K.S.R. T.R.J.
810 developed the methodology for quantifying the effect of seasonal accumulation on water isotope diffusion using the
811 CFM and chemistry data. T.J.F. and M.S. provided chemistry data. J.G. assisted with the development of the water
812 isotope dataset over depths of 1035.4 to 1368.2 m, and J.G. and K.S.R. assisted with data quality control. All authors
813 discussed the results and contributed input to the manuscript.

814

815 **Author Information**

816 Reprints and permissions information is available at www.nature.com/reprints. The authors declare no competing
817 financial interests. Readers are welcome to comment on the online version of the paper. Correspondence and
818 requests for materials should be addressed to T.R.J. (tyler.jones@colorado.edu)